Microporous Carbon Nanoplates from Regenerated Silk Proteins for Supercapacitors

Young Soo Yun, Se Youn Cho, Jinyong Shim, Byung Hoon Kim, Sung-Jin Chang, Seung Jae Baek, Yun Suk Huh, Yongsug Tak, Yung Woo Park, Sungjin Park, and Hyoung-Joon Jin*

Supercapacitors, also known as electrochemical capacitors or ultracapacitors, have attracted much attention because of their high power capability, good reversibility, and long cycle life.[1–4] Since high power delivery and uptake (10 kW/kg) can be achieved in as little as a few seconds, supercapacitors have had an important role in complementing or replacing batteries in various energy storage fields such as electric vehicles, mobile phones, and uninterruptible power supplies for computers.[1–4] However, the energy density (about 5 Wh/kg) of supercapacitors is lower than that of batteries,[1] which limits their adoption for those applications. Supercapacitors can be classified into two categories with respect to their energy storage mechanisms. One is the electric double-layer capacitor (EDLC), where the capacitance comes from the pure electrostatic charge accumulated at the electrode/electrolyte interface. It requires electrode materials with high surface area and pores adapted to the size of ions.[5–7] The other category is the pseudocapacitor, in which fast and reversible faradic processes take place due to electroactive species.[5] Metal oxides, such as RuO_2 or MnO_2, and electrically conductive polymers have been used to increase specific capacitance *via* pseudocapacitive redox reactions.[8–13] However, poor cycle stability, low electrical conductivity and high price have limited the practical application of pseudocapacitive materials. Recently, EDLC-based materials with pseudocapacitive effects have been reported.[14–18] The incorporation of heteroatoms into carbon materials has brought about considerable improvement of specific capacitance because the heteroatoms induce pseudocapacitive behaviour and improve the polar properties of carbon materials. The maximum power density of a supercapacitor is given by $P_{max} = V_i^2/(4R)$, where V_i is the initial voltage, and R is the equivalent series resistance (ESR). Because of this the resistivity of the electrode becomes a key factor in determining the power of the supercapacitor. The maximum storage energy is given by $CV_i^2/2$, where C is the capacitance; therefore, maximizing the capacitance of an electrode is the key way to increase energy density.[19,20]

Silk produced by the *B. mori* silkworm is one of the most abundant polymers in nature, which are cultivated more than 480000 ton per year all over the world.[21] It is composed of fibrous proteins, known as fibroin, and sericin that surrounds the fibroin fibers and cements them together. Silk fibroin was dissolved and then reformulated into new materials (regenerated silk fibroin).[22,23] The cast film obtained from regenerated silk fibroin reveals multiple layers induced by swelling with a layer thickness of ~150 nm.[23] This result suggests that carbon-based nanoplates can be prepared from regenerated silk fibroin by carbonization. In this study, novel carbon-based microporous nanoplates containing numerous heteroatoms (H-CMNs) were fabricated from regenerated silk fibroin. A high surface area was induced by KOH activation during carbonization. Consequently, H-CMNs possess potential advantages for application in supercapacitor electrodes with high energy and power density.[1,24,25]

As shown in **Figure 1**a, solutions of regenerated silk fibroin were prepared by dissolving degummed natural cocoons using a concentrated aqueous solution of lithium bromide (9.3 M). As-casted regenerated silk fibroin films were carbonized from room temperature to 800 °C for holding time of 3 hours under a heating rate of 5 °C/min and an Ar flow of 200 mL/min. Carbon flakes with a glittering surface were obtained by carbonization of the as-casted regenerated silk fibroin films. The resulting material has numerous heteroatoms such as nitrogen

Y. S. Yun, S. Y. Cho, Prof. H.-J. Jin
Department of Polymer Science and Engineering
Inha University
Incheon 402-751, South Korea
Fax: (+82) 32-865-5178
E-mail: hjjin@inha.ac.kr
J. Shim, Prof. Y. Tak
Department of Chemical Engineering
Inha University
Incheon 402-751, South Korea
Prof. B. H. Kim
Department of Physics
University of Incheon
Incheon 406-772, Republic of Korea
Dr. S.-J. Chang
Division of Materials Science
Korea Basic Science Institute (KBSI)
Daejeon 305-333, South Korea
S. J. Baek, Prof. Y. W. Park
Department of Physics and Astronomy
and Department of Nano Science and Technology,
Seoul National University
Seoul 151-747, South Korea
Prof. Y. S. Huh
Department of Biological Engineering
Inha University
Incheon 402-751, South Korea
Prof. S. Park
Department of Chemistry
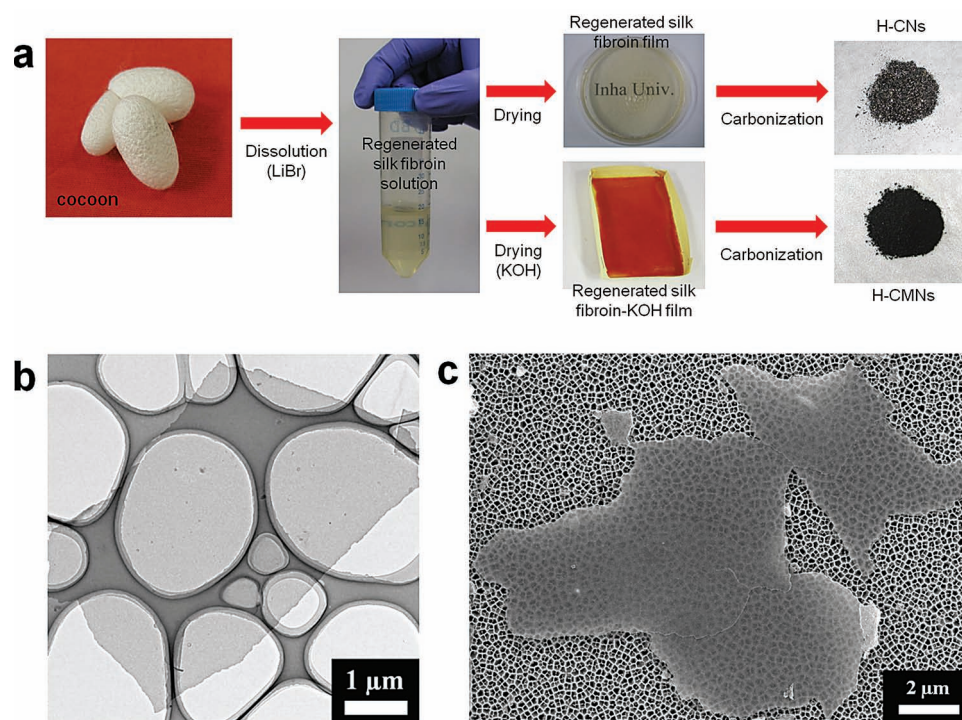Inha University
Incheon 402-751, South Korea

Figure 1. Schematic images and morphologies of the H-CMNs. a) Fabrication process of the H-CMNs. Silk fibroin fibers degummed from natural cocoons were dissolved in LiBr (9.3 M), and then as-casted regenerated silk fibroin film and regenerated silk fibroin-KOH film were carbonized. b) FE-TEM image of the H-CMNs on a holey carbon grid. c) FE-SEM image of the H-CMNs on alumina template membranes.

and oxygen and lateral size greater than 5 μm and thickness less than < 100 nm. The heteroatom doped carbon-based nanoplates (H-CNs) were exfoliated from the carbon flakes by ultrasonication in organic solvents, such as N-methyl-pyrrolidone (Figure S1).[26] Schematic models of the *B. mori* silk fibroin lamellar-like layer formation in water by self-assembly are shown in **Figure 2**. The silk fibroin film cast from silk solution had a lamellar-like layer structure with a layer thickness of about 150 nm. The lamella-like layer structure is induced from self-assembly of the hydrophobic and hydrophilic blocks of silk fibroin in aqueous system.[27] Then, the layer structure of silk fibroins was stacked each other into the thin film.[23] The layer structure was maintained in the thermal annealing process at 200 °C, which is above glass transition temperature (Figure 2a). Noncrystalline random coil structures of the silk fibroin film were transformed into β-sheet crystal-dominant structures above the glass transition temperature (Figure S2). This fact indicates that a β-sheet crystal-dominant, lamellar-like layer structure was formed after thermal annealing. The β-sheet crystal-dominant, lamella-like layer structure can be transformed to carbon materials by structural transformation like cyclization.[28,29] H-CMNs were fabricated by carbonization of the as-casted regenerated silk fibroin-KOH films. This KOH treatment brought about remarkable differences between H-CNs and H-CMNs. It is suggested that the activation of carbon with KOH proceeds as $6KOH + C \leftrightarrow 2K + 3H_2 + 2K_2CO_3$, followed by decomposition of K_2CO_3 and/or reaction(s) of $K/K_2CO_3/CO_2$ with carbon.[2,30,31] The H-CMNs had a flat nanoplate structure as shown in Figure 1b and c.

Figure 3a shows a topographic image of the H-CMN observed by atomic force microscopy (AFM). Figure 3b shows a height-profile of the white dot line in Figure 3a. A rough surface could be induced by the activation of KOH, which, compared to steam activation, brings about a higher surface area and more needle-like narrow pores that are advantageous in charge storage. Figure 3c shows the Raman spectra of the H-CMNs. The peak positions of the *D*, *G*, and *2D* bands are ~1361, ~1600 and ~2746 cm^{-1}, respectively. Also, the ratio of the *D* peak intensity to the *G* peak intensity and the ratio of the *2D* peak intensity to the *G* peak intensity are ~1 and ~0.17, respectively. D/G ratio (~1) and 2D/G ratio (~0.17) in peak intensity are similar to the typical values for graphene oxide nano-platelets.

The Brunauer-Emmett-Teller (BET) specific surface area of the H-CMNs was 2557.3 m^2/g, which is similar to the theoretical surface area of pristine graphene sheet. In contrast, H-CNs had low surface area below 30 m^2/g and their exfoliation was not easy. The activation agent, KOH, to regenerated silk fibroin weight ratio affected the specific surface area of the H-CMNs (Figure S3). When the weight ratio (regenerated silk fibroin/ KOH) weight ratio was 1, its surface area was the highest among the samples produced in this work. As the amount of the activation agents was increased, the micropore-to-mesopore ratio was increased. Although micropores were formed by the activation agents on the surface, too much of the activation agents resulted in unfavorable effects. This result suggested the absence of any linear relation between the activation agent content and the micropore surface area. However, the nitrogen adsorption and desorption isotherm curves of all the samples
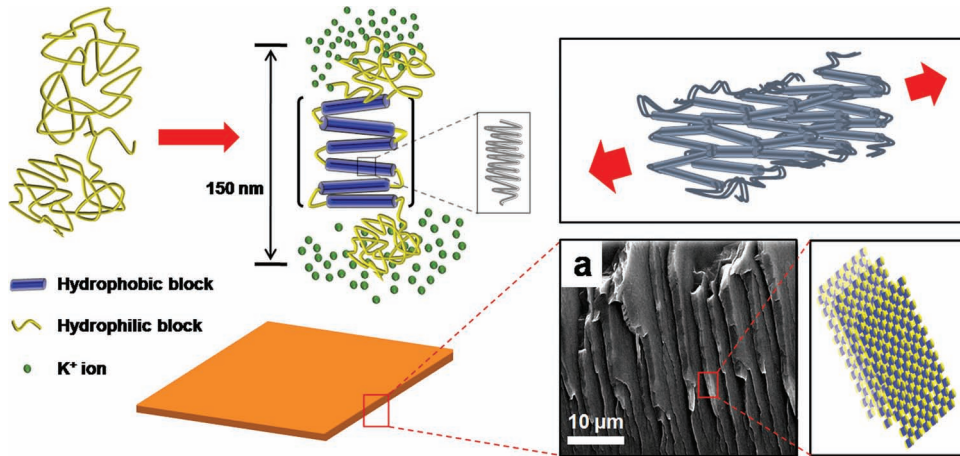
Figure 2. Schematic model of *Bombyx mori* silk fibroin lamellar-like layer formation in water by self-assembly. a) SEM image of regenerated silk fibroin film after thermal treatment at 200 °C.

with various regenerated silk solutions and activation agent weight ratios showed an IUPAC type- I microporous structure (Figure S3), and the pore-size distributions of nanopores were also similar (Figures S4). The size of nanopores formed was less than 4 nm, and most of the mesopores was several nanometers in diameter (inset of Figure 3d). On the top of its high surface area, the H-CMNs have numerous heteroatoms such as oxygen and nitrogen as shown in Figure S5 and Table S1. Furthermore, electrical conductivity of the H-CMNs is ~ 1.15×10^4 S/m, which is comparable to that of highly doped silicon (Figures S6-8).
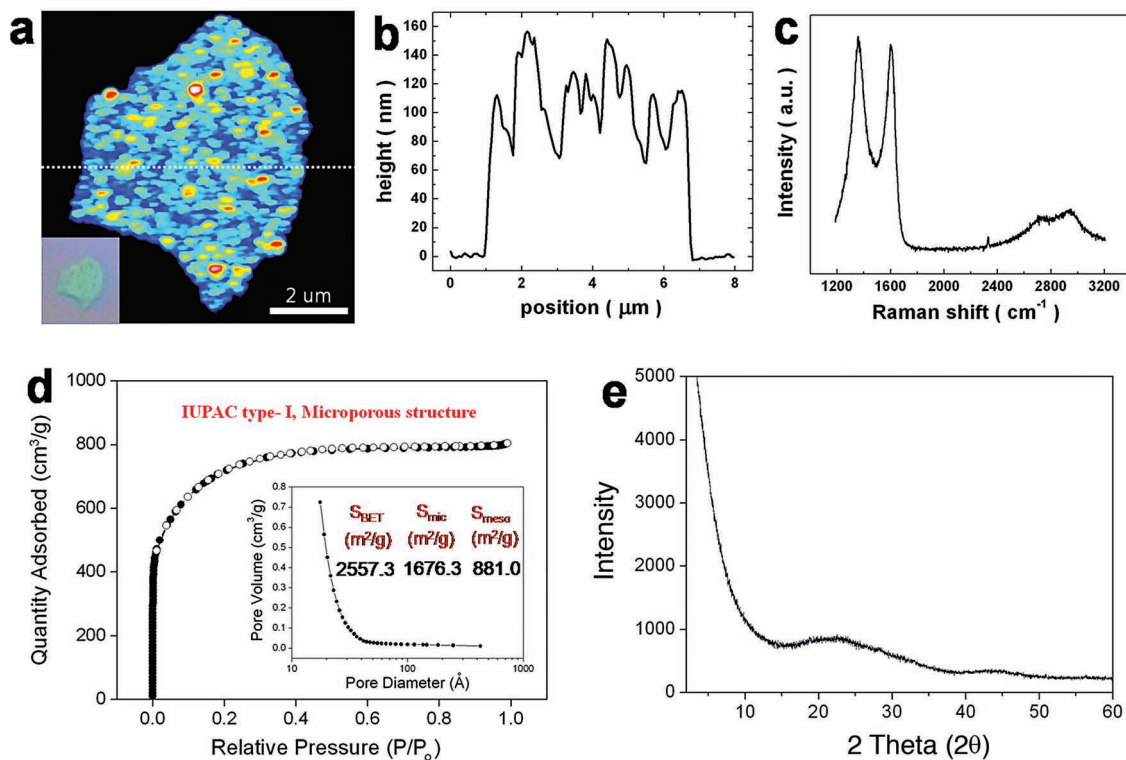

Figure 3. Charaterization of the H-CMNs. a) Topographic image and optical microscope image of the H-CMNs. The H-CMNs had a rough surface area induced by activation of KOH. b) the line-profile of the white dot line in Figure 2a. c) Raman spectrum of the H-CMNs typically observed in the given samples. *D*, *G*, and 2*D* bands are confirmed at ~1361, ~1600 and ~2746 cm⁻¹. d) Nitrogen adsorption and desorption isotherm curve and pore-size distribution (inset) of the H-CMNs from regenerated silk fibroin and KOH weight ratio of 1:1. The curve exhibits IUPAC type- I microporous structure, and nanopores below 4 nm are well-developed. The specific surface area of 2557.3 m²/g with a micropore surface area of 1676.3 m²/g and a mesopore surface area of 881.0 m²/g. e) XRD pattern of the H-CMNs. XRD peaks at 22.5 and 43.8 were observed, exhibiting a amorphous carbon structure. In addition, a large intensity increase in the low-angle scatter shows the presence of a high density of micropores.
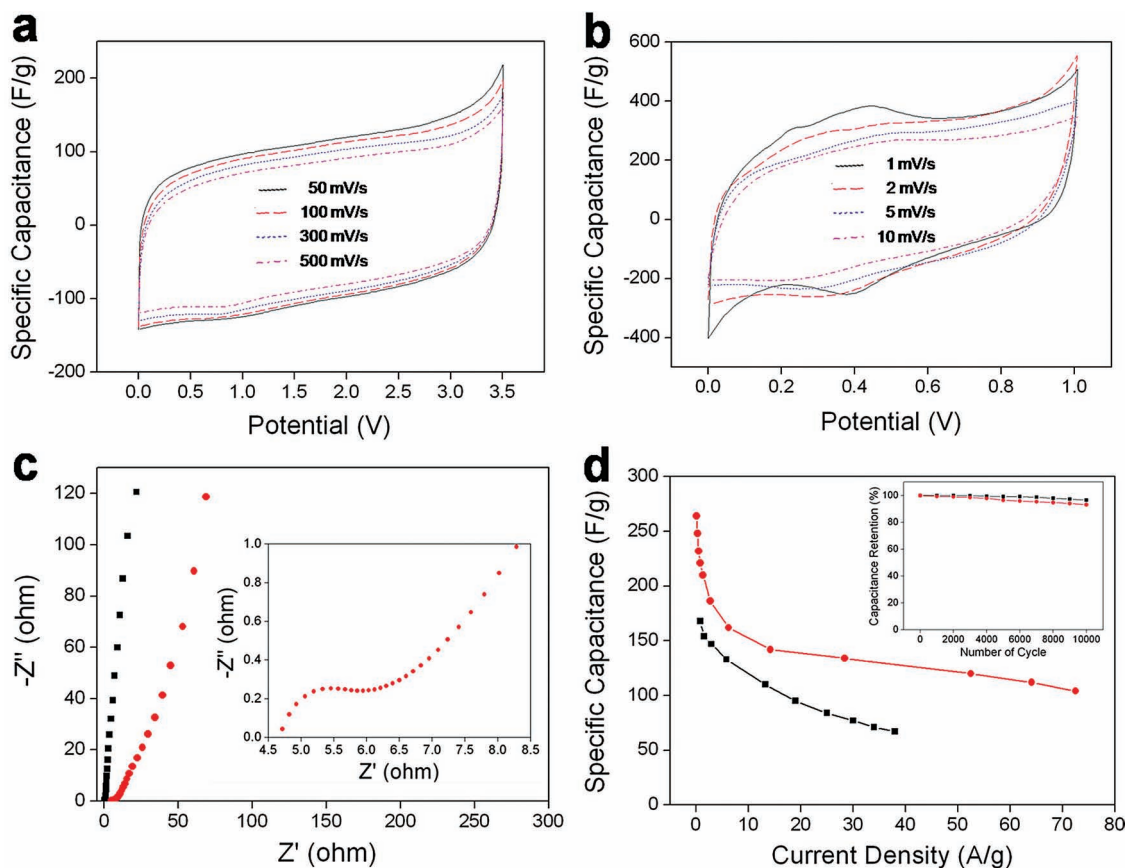
Figure 4. Electrochemical performance of the H-CMNs. a) Cyclic voltammograms of the HCMNs at scan rates of 50, 100, 300, and 500 mV/s over a potential range from 0 to 3.5 V in the BMIM BF$_4$/AN electrolyte. b) Cyclic voltammograms of the H-CMNs at scan rates of 1, 2, 5, and 10 mV/s over a potential range from 0 to 1 V in 1 M H$_2$SO$_4$ electrolyte. c) Nyquist plots of the H-CMNs in the frequency range from 100 kHz to 0.1 Hz (square in BMIM BF$_4$/AN electrolyte and circle in 1 M H$_2$SO$_4$ electrolyte). High frequency range data (inset) exhibits presence of a semicircle according to the faradic charge-transfer resistance. d) Specific capacitances at various current densities measured in organic and aqueous electrolytes. Capacitance retention (inset) measured in both organic and aqueous electrolytes.

Figure 3e shows the characterization of the H-CMNs by means of X-ray diffraction (XRD). Peaks around 22.5 and 43.8° of 2 theta could be assigned the (100) plane according to the fabrication of the amorphous carbon structures. In addition, a large intensity increase in the low-angle scatter is consistent with the presence of a high density of micropores.

The electro-chemical performance of the H-CMNs was analyzed in both organic electrolyte, 1-butyl-3-methylimidazolium tetrafluoroborate (BMIM BF$_4$)/acetonitrile (AN), and aqueous electrolyte, 1 M H$_2$SO$_4$. **Figure 4**a shows cyclic voltammograms of the H-CMNs in the BMIM BF$_4$/AN electrolyte. The samples exhibited a typical capacitive behaviour with rectangular shaped voltammetry characteristics from 0 to 3.5 V over a wide range of voltage scan rates. However, in the 1 M H$_2$SO$_4$ electrolyte, the cyclic voltammogram curves exhibited humps as well as a rectangular shape, indicating that the capacitive response results from the combination of electrical double-layer formation and redox reactions, which are related to the heteroatom functionalities of the materials (Figure 4b). Figure 4c shows Nyquist plots of the H-CMNs (squares indicate BMIM BF$_4$/AN electrolyte, and circles indicate 1 M H$_2$SO$_4$ electrolyte) in a frequency

range from 100 kHz to 0.1 Hz. The equivalent series resistance (ESR) of the H-CMNs in the BMIM BF$_4$/AN electrolyte is 0.62 Ω, which is estimated from the value of the real axis at 448 Hz. This value is much smaller than 6.2 Ω in the 1 M H$_2$SO$_4$ electrolyte. The difference in the ESRs is due to the ionic resistance associated with the migration of electrolyte ions. The curve in the 1 M H$_2$SO$_4$ electrolyte shows a semicircle in the high-frequency region. The semicircle in the high-frequency range is associated with the surface properties of the porous electrode and corresponds to the faradic charge-transfer resistance. Therefore, the semicircle in the 1 M H$_2$SO$_4$ electrolyte indicates that the pseudocapacitive behaviour of nitrogen and oxygen heteroatoms contributed to the electro-chemical performance. This result coincides with the cyclic voltammogram data of Figure 4b. In the low-frequency region, the imaginary component of the impedance plots represents the capacitive behaviour. In the case of the electric double-layer capacitor, the impedance plot should theoretically be a vertical line parallel to the imaginary axis. The impedance plot with BMIM BF$_4$/AN electrolyte followed the capacitive behaviour, however that with 1 M H$_2$SO$_4$ electrolyte did not. The specific capacitance of the H-CMNs in

the 1 M H_2SO_4 electrolyte was 264 F/g on the discharge curve with a constant current of 0.1 A/g. At a current density of 6.2 A/g, the capacitance value is 162 F/g which is not an exceptional value for H_2SO_4 medium. However, at a current density of 52.5 A/g, the capacitance value is 120 F/g which is a superb result. Also, even over 70 A/g, a capacitance greater than 100 F/g was maintained (Figure 4d). The superb capacitance of the H-CMNs had several causes. First, the H-CMNs had a large amount of open micropores on the surface. Second, heteroatoms, such as nitrogen and oxygen, induced pseudocapacitive behaviour and improved the polar properties of the H-CMNs. Third, the H-CMNs had a high surface area and a topographically rough surface, which can obstruct dense agglomeration and extend the electrochemical interface due to the pore geometry's advantageous performance in contact formation in the electrolyte. Also, the surface area of the H-CMNs can be fully utilized in electrochemical reactions due to the absence of an area blocked by dense agglomeration and hydrophobicity. Therefore, electrochemical performances of the H-CMNs could be better than activated native silk fibers.[32] In addition, the H-CMNs exhibited an excellent electrochemical stability in a wide range of working voltage of 3.5 V despite a presence of numerous heteroatoms. The specific capacitance of the H-CMNs in the BMIM BF_4/AN electrolyte was 168 F/g on the discharge curve with a constant current of 0.8 A/g and a working voltage of 3.5 V (Figure 4d). The energy density and power density reached 133 Wh/kg and 217 kW/Kg, respectively (Figure S9). The energy density of the H-CMNs comparable to that of Li-ion batteries, and the power density is several orders higher than that of Li-ion batteries. This results from the high capacitance and good electrical properties of the H-CMNs. In addition, capacitor cells using the H-CMNs were very stable in repetitive cycles. After 10000 constant current charge/discharge cycles at a current density of 2.5 A/g in the BMIM BF_4/AN and 1 M H_2SO_4 electrolytes, the capacitance values decreased to only 3.5% and 6.8% of the initial capacitance, respectively, demonstrating that H-CMNs have good cycle stability (Figure 4d inset).

In summary, the H-CMNs were fabricated by regenerated silk fibroin, unique organic precursor, and KOH mixtures. The H-CMNs had high surface areas, morphological characteristics advantageous in contacts to electrolyte, large amount of nanopores effective in double-layer formations, good electrical property, and numerous heteroatoms. These superior characteristics could result in high electrochemical performances, displaying a specific capacitance of 264 F/g in aqueous electrolytes, a specific energy of 133 Wh/kg, a specific power of 217 kW/kg, and a stable cycle life over 10000 cycles.

Experimental Section

Preparation of aqueous solutions of silk fibroin: *B. mori* silk fibroin solutions were prepared using a modification of the procedure reported elsewhere.[22] Cocoons of *B. mori* silkworm silk were boiled for 30 min in an aqueous solution of Na_2CO_3 (OCI company, 99%, 0.02 M) and rinsed thoroughly with water to remove the glue-like sericin proteins. The extracted silk was then dissolved in a 9.3 M LiBr (Sigma-Aldrich, ≥ 99%) aqueous solution at room temperature to yield a 20 wt% solution. This solution was dialyzed in water using Slide-a-Lyzer dialysis cassettes (Pierce, MWCO 3500) for 48 h. The final concentration of the aqueous silk fibroin solution was 7.0 to 8.0 wt%.[23]

Preparation of the H-CMNs from regenerated silk fibroin-KOH films: Various quantities of potassium hydroxide (4, 6.4, 8, and 16 g) were added to 100 g samples of the aqueous silk fibroin solution. The silk fibroin solutions containing KOH were stirred for 30 min and were then cast in Teflon dishes. The cast solutions were dried in a convection oven at 120 °C for 3 days. The product films were carbonized from room temperature to 800 °C for 3 hours. A heating rate of 5 °C/min and an Ar flow of 200 mL/min were applied. The product (H-CMNs) were washed using distilled water and ethanol (OCI company, 99.9%) and were then dried in a vacuum oven at 30 °C.

Electrochemical performance of the H-CMNs: A two-electrode cell configuration was used to measure the performance of the H-CMNs as an electrode for supercapacitors. For the aqueous system, 5 wt% of polytetrafluoroethylene (PTFE, Sigma-Aldrich, 60 wt% dispersion in H_2O) was added to the H-CMNs as a binder. Typically, the H-CMNs and PTFE were mixed into a paste using a mortar and pestle, rolled into uniform thickness sheets whose thickness ranged from 40 to 50 μm (from sheet to sheet), and punched into 1 cm diameter electrodes. For the non-aqueous system, the H-CMNs were mixed into a paste with 5 wt% of poly-vinylidene fluoride.

The electrodes were formed from a thick slurry and pressed onto the conductive carbon-coated aluminum current collector. Each electrode had a diameter of 1 cm and a thickness of approximately 100 μm. A typical pair of electrodes had a weight between 2.5 and 3.0 mg after drying overnight at 100 °C. 1 M H_2SO_4 (OCI company, 95%) was used as an aqueous electrolyte, and for a non-aqueous electrolyte, BMIM BF_4 was obtained commercially from Sigma Aldrich and diluted in AN with a weight ratio of 1:1. The electrodes and a porous polypropylene separator (Whatman GF/D) were sandwiched together in a stainless steel cell for the fully assembled two-electrode cell device. All steps in the cell preparation were done in an argon-filled glove box (oxygen and water contents below 1 ppm, respectively).

Electrochemical data were obtained using cyclic voltammetry, chronopotentiometry, and electrical impedance spectroscopy (EIS) (PGSTAT302N, Autolab). Capacitance, energy density, and power density were all characterized by galvanostatic measurements. A current ranging from 0.1 to 70 A/g was applied to the cells, while potentials between both electrodes were swept between cutoff values (0 to 1 V in the aqueous system, 0 to 3.5 V in the non-aqueous system). For the cycling test in both systems, 2.5 A/g was applied.

Characterization: The morphologies of the H-CMNs were observed by field emission transmission electron microscopy (FE-TEM; JEM2100F, JEOL, Japan) equipped with an energy-dispersive X-ray, field emission scanning electron microscopy (FE-SEM; S-4300, Hitachi, Japan) and AFM (a Digital Instrument Nanoscope IVA). The porous properties of the H-CMNs were analyzed using nitrogen adsorption and desorption isotherms that were obtained using the surface area and a porosimetry analyzer (ASAP 2020, Micromeritics, USA) at −196 °C. The BET surface areas (S_{BET}) were calculated according to the Brunauer-Emmett-Teller (BET) theory. The micropore surface area (S_{mic}) was obtained using t-plot theory, whereas the mesopore surface area (S_{meso}) was calculated according to the Barrett-Johner-Halendar theory. XRD (Rigaku DMAX 2500) analysis of the H-CMNs was performed using Cu Kα radiation (wavelength $\lambda = 0.154$ nm) operated at 40 kV and 100 mA. Elemental analysis was performed using an EA1112 (CE instrument, Italy). XPS (PHI 5700 ESCA) analysis was performed using monochromated Al Kα radiation (hv = 1486.6 eV). A commercially available cantilever, NSG-10 (NT-MDT, Russia) was used under semi-contact operation mode for AFM. For Raman spectroscopy, a continuous-wave linearly polarized laser with a wavelength of 473 nm (2.62 eV), a pinhole of 50 μm, and a 600 grooves/mm grating were used. To ensure nondestructive measurements, low laser power was used (<300 μW, on the sample).

Supporting Information

Supporting Information is available from the Wiley Online Library or from the author.

COMMUNICATION

[1] P. Simon, Y. Gogotsi, *Nat. Mater.* **2008**, *7*, 845.

[2] Y. Zhu, S. Murali, M. D. Stoller, K. J. Ganesh, W. Cai, P. J. Ferreira, A. Pirkle, R. M. Wallace, K. A. Cychosz, M. Thommes, D. Su, E. A. Stach, R. S. Ruoff, *Science* **2011**, *332*, 1537.

[3] J. R. Miller, P. Simon, *Science* **2008**, *321*, 651.

[4] Y. Zhang, H. Feng, X. Wu, L. Wang, A. Zhang, T. Xia, H. Dong, X. Li, L. Zhang, *Int. J. Hydrogen Energy* **2009**, *34*, 4889.

[5] L. L. Zhang, X. S. Zhao, *Chem. Soc. Rev.* **2009**, *38*, 2520.

[6] J. Chmiola, G. Yushin, Y. Gogotsi, C. Portet, P. Simon, P. L. Taberna, *Science* **2006**, *22*, 1760.

[7] J. Chmiola, C. Largeot, P. L. Taberna, P. Simon, Y. Gogotsi, *Angew. Chem. Int. Ed.* **2008**, *47*, 3392.

[8] Z.-S. Wu, D.-W. Wang, W. Ren, J. Zhao, G. Zhou, F. Li, H.-M. Cheng, *Adv. Funct.Mater.* **2010**, *20*, 3595.

[9] X. Liu, P. G. Pickup, *J. Power Sources* **2008**, *176*, 410.

[10] S. Chen, J. Zhu, X. Wu, Q. Han, X. Wang, *ACS Nano* **2010**, *4*, 2822.

[11] X. Xie, L. Gao *Carbon* **2007**, *45*, 2365.

[12] Q. Wu, Y. Xu, Z. Yao, A. Liu, G. Shi, *ACS Nano* **2010**, *4*, 1963.

[13] J. Jang, J. Bae, M. Choi, S.-H. Yoon, *Carbon* **2005**, *43*, 2730.

[14] D. Hulicova-Jurcakova, M. Seredych, G. Q. Lu, T. J. Bandosz, *Adv. Funct. Mater.* **2009**, *19*, 438.

[15] Y. S. Yun, J. Shim, Y. Tak, H.-J. Jin, *RSC Adv.* **2012**, *2*, 4353.

[16] L. Zhao, L.-Z. Fan, M.-Q. Zhou, H. Guan, S. Qiao, M. Antonietti, M.-M. Titirici, *Adv. Mater.* **2010**, *22*, 5202.

[17] H. M. Jeong, J. W. Lee, W. H. Shin, Y. J. Choi, H. J. Shin, J. K. Kang, J. W. Choi, *Nano Lett.* **2011**, *11*, 2472.

[18] S. Park, Y. Hu, J. O. Hwang, E.-S. Lee, L.B. Casabianca, W. Cai, J. R. Potts, H.-W. Ha, S. Chen, J. Oh, S. O. Kim, Y.-H. Kim, Y. Ishii, R. S. Ruoff, *Nat.Commun.* **2012**, *3*, 638.

[19] C. Du, N. Pan, *Nanotechnology* **2006**, *17*, 5314.

[20] K. H. An, W. S. Kim, Y. S. Park, J.-M. Moon, D. J. Bae, S. C. Lim, Y. S. Lee, Y. H. Lee, *Adv. Funct. Mater.* **2001**, *11*, 387.

[21] http://faostat3.fao.org/

[22] A. Motta, L. Fambri, C. Migliaresi, *Macromol. Chem. Phys.* **2002**, *203*, 1658.

[23] H.-J. Jin, J. Park, V. Karageorgiou, U.-J. Kim, R. Valluzzi, P. Cebe, D. L. Kaplan, *Adv. Funct. Mater.* **2005**, *15*, 1241.

[24] E. Raymundo-Piñero, K. Kierzek, J. Machnikowski, F. Béguin, *Carbon* **2006**, *44*, 2498.

[25] E. Frackowiak, F. Béguin, *Carbon* **2001**, *39*, 937.

[26] Y. Hernandez, V. Nicolosi, M. Lotya, F. M. Blighe, Z. Sun, S. De, I. T. Mcgovern, B. Holland, M. Byrne, Y. K. Gunko, J. J. Boland, P. Niraj, G. Duesberg, S. Krishnamurthy, R. Goodhue, J. Hutchison, V. Scardaci, A. C. Ferrari, J. N. Coleman, *Nat. Nanotechnol.* **2008**, *3*, 563.

[27] H.-J. Jin, D. L. Kaplan, *Nature* **2003**, *424*, 1057.

[28] J. E. Bailey, A. J. Clarke, *Nature* **1971**, *234*, 529.

[29] W. Watt, W. Johnson, *Nature* **1975**, *257*, 210.

[30] M. A. Lillo-Ródenas, D. Cazorla-Amorós, A. Linares-Solano, *Carbon* **2006**, *41*, 267.

[31] E. Raymundo-Piñero, P. Azais, T. Cacciaguerra, D. Cazorla-Amorós, A. Linares-Solano, F. Béguin, *Carbon* **2005**, *43*, 786.

[32] Y. J. Kim, Y. Abe, T. Yanagiura, K. C. Park, M. Shimizu, T. Iwazaki, S. Nakagawa, M. Endo, M. S. Dresselhaus, *Carbon* **2007**, *45*, 2116.